

Layer-dependent electronic structures and magnetic ground states of polar-polar $\text{LaVO}_3/\text{KTaO}_3(001)$ heterostructures

Shubham Patel ^{1,*}, Narayan Mohanta ², Snehasish Nandy,^{3,4} Subhendra D. Mahanti ⁵ and A. Taraphder ^{1,†}

¹*Department of Physics, Indian Institute of Technology, Kharagpur 721302, India*

²*Department of Physics, Indian Institute of Technology Roorkee, Roorkee 247667, India*

³*Theoretical Division, Los Alamos National Laboratory, Los Alamos, New Mexico 87545, USA*

⁴*Department of Physics, National Institute of Technology, Silchar, Assam 788010, India*

⁵*Department of Physics and Astronomy, Michigan State University, East Lansing, Michigan 48824, USA*



(Received 9 December 2023; revised 22 May 2024; accepted 18 July 2024; published 1 August 2024)

Employing a first-principles and model Hamiltonian approach, we work out the electronic properties of polar-polar $\text{LaVO}_3/\text{KTaO}_3$ (LVO/KTO, 001) heterostructures, with up to six layers of KTO and five layers of LVO. Our analyses indicate the existence of multiple Lifshitz transitions (LTs) within the t_{2g} bands, which can be fine-tuned by adjusting the number of LVO layers or applying gate voltage. Contrary to the experimental report, spin-orbit coupling is found to be negligible, originating solely from the Ta $5d_{xy}$ -derived band of KTO, while the $5d_{xz}$ and $5d_{yz}$ bands are considerably away from the Fermi level while LVO overlayers having no role in it. Magnetic properties of the heterostructures, due to vanadium ions, exhibit a pronounced sensitivity to the number of LVO and KTO layers. Our calculations indicate that the interlayer AFM, (so called A-AFM), is energetically most favorable. This is further supported by ground state energy calculations on extended $\sqrt{2} \times \sqrt{2}$ supercells. Moreover, we find that an insulator to metal transition at the interface requires four LVO layers, corroborating the experimental observation. The interfaces featuring ferromagnetic (FM) ground states turn out to be *half-metallic* after the critical thickness is reached. Considerations of the magnetic interactions appear crucial for the experimentally observed critical thickness for metallicity.

DOI: [10.1103/PhysRevB.110.054402](https://doi.org/10.1103/PhysRevB.110.054402)

I. INTRODUCTION

Interfaces of polar-nonpolar perovskite heterostructures are well-studied in literature owing to various applications using their physical properties such as the formation of a two-dimensional electron gas (2DEG), metal-insulator transition, magnetotransport, magnetism, and superconductivity [1–3]. The next generation perovskite heterostructure is polar-polar where due to ionic interactions, an intrinsic electric field is induced [4,5]. The ability to tune the physical and chemical properties of a system by an external electric field along with the induced internal electric field is a major objective of electronic, optoelectronic, and nanoelectronic applications.

A wide variety of interfaces have been extensively investigated both experimentally and theoretically; in particular, a well-known polar-nonpolar $\text{LaAlO}_3/\text{SrTiO}_3$ (LAO/STO) (001) interface has emerged as a promising candidate for last few decades due to its remarkable features. It exhibits LAO thickness-dependent transport properties, absent in its bulk counterparts [6–8]. Other than the metal-insulator transition, the Rashba spin-splitting [9,10], the coexistence of ferromagnetism and superconductivity [3,10,11], electronic reconstruction [8], oxygen-vacancy effects [12], topological superconductivity [13,14], and its influence on Lifshitz transitions [15] are explored in these interfaces. Notably, a critical

thickness of four unit cells of LAO is necessary to make the interface conducting [7]. Compared to the polar-nonpolar interfaces, which form the 2DEG via polar discontinuity, the polar-polar oxide interfaces [5] are expected to produce higher charge carrier density and carrier mobility as there are, in principle, two electron-donor layers in this case transferring electrons to the interface to avoid polar discontinuity [16].

In a recent experimental report, such a polar-polar interface is formed to study its transport properties, in which the layers of LaVO_3 are stacked over KTaO_3 a substrate, forming a $\text{LaVO}_3/\text{KTaO}_3$ (LVO/KTO) interface in (001) direction [4]. A strong anisotropic transverse and longitudinal magnetoresistance (MR) was interpreted as the signature of strong spin-orbit coupling (SOC). In addition, the nature of observed anomalous MR (AMR) and planar-Hall effect (PHE) [17] was thought to come from Weyl fermions. The bulk KTaO_3 is a band insulator with an optical gap of 3.5 eV [18,19] crystallizing in a cubic symmetry with space group 221 ($\text{Pm}\bar{3}\text{n}$). It has a sizable SOC strength compared to SrTiO_3 coming from the Ta $5d$ orbitals [20–22]. ABO_3 oxides form alternative (+/–) charges in (AO) and BO_2 layers. In case of KTaO_3 , the sequence is $(\text{K}^+\text{O}^{2-})^{-1}/(\text{Ta}^{5+}\text{O}_2^{2-})^{+1}$, while it is $(\text{La}^{3+}\text{O}^{2-})^{+1}/(\text{V}^{3+}\text{O}_2^{2-})^{-1}$ for LaVO_3 . Unlike LAO/STO, in LVO/KTO, the two materials form a ++ interface of $(\text{TaO}_2)^{+1}/(\text{LaO})^{+1}$ type, when terminated at TaO_2 .

Electron-electron correlations are usually considered important in d -electron systems for the metal-insulator transition (MIT) and the experimentally observed band gap. However, this is not always the case. As discussed in recent

*Contact author: spatelphy@iitkgp.ac.in

†Contact author: arghya@phy.iitkgp.ac.in

theoretical studies [23,24], microscopic degrees of freedom such as structural distortions and magnetic order actively participate in breaking local symmetries. Such symmetry breaking (SB) could indeed lead to MIT. Lowering the lattice symmetry can lower overall energy, and lead to a more stable state. In addition, formation of a heterostructure lowers the energy compared to the sum of energies of the participating bulk materials. This specific class of materials is in polymorphous crystal geometries, in which local and global symmetries are not the same, as discussed by Malyi *et al.* [24]. As we will show, in LVO/KTO systems we have studied, even though the structural and magnetic SBs are important, we find that the stabilization of the insulating phase requires electronic correlation via Hubbard-like U .

To address the issue of a conducting interface, and consequently, the formation of 2DEG, we investigate the electronic properties of the polar-polar (001) LVO/KTO interface using first-principles density functional calculations. The cubic LaVO_3 (LVO), which is metallic with mostly V $3d$ orbitals at the Fermi level (FL), forms a conducting interface with KTO substrate even with a single layer of LVO. Although it is unclear from the experimental report which structure of LVO was used for the transport investigation, the charge distribution in the thin films of LVO and a later study suggest that a cubic LVO was likely used to form the LVO/KTO interface [25]. We therefore perform our investigations with cubic LVO [26,27] to match the stoichiometry and structure of KTO. In passing, we note that the orthorhombic phase of LaVO_3 is a Mott-Hubbard insulator [28,29], undergoing a metal-insulator transition [30,31]. The cubic perovskite LVO is a ferromagnetic metal with a total magnetic moment $\sim 2\mu_B$, as reported by Rashid *et al.* [32]. To the best of our knowledge, no previous studies discuss the magnetic order in LVO-based heterostructures, except one experiment [33]. There are also some theoretical studies dedicated to the cubic phase of bulk LVO, investigating the magnetism [32] and electron-correlation using DMFT [34,35]. Along with the nonmagnetic calculations, we also report various possible magnetic orders with different number of layers of LVO in the LVO/KTO heterostructure.

The remainder of the paper is organized as follows. In Secs. II and III, we describe the computational details and the interface geometry, respectively. In Sec. IV, we present the nonmagnetic electronic band structures with different layers of LVO and KTO, and then in Sec. V we discuss the possible magnetic ordering in the LVO layers. Finally, in Sec. VII, we conclude with our findings.

II. METHODOLOGY

We use density functional theory as implemented in Vienna *ab initio* simulation package (VASP) within the plane-wave pseudopotential method [36,37]. To approximate the electron-ion potential, we use the projected wave method [38], and the Perdew-Burke-Ernzerhof of the generalized gradient approximation [39] is used to approximate exchange-correlation effects, taking into account the on-site Coulomb interactions (GGA + U) for La, Ta and V within Dudarev's approach [40]. An empirical U value equal to 7.5 eV is used for La [41], while for Ta and V it is 5 eV [42] and 3.4 eV [43], respectively.

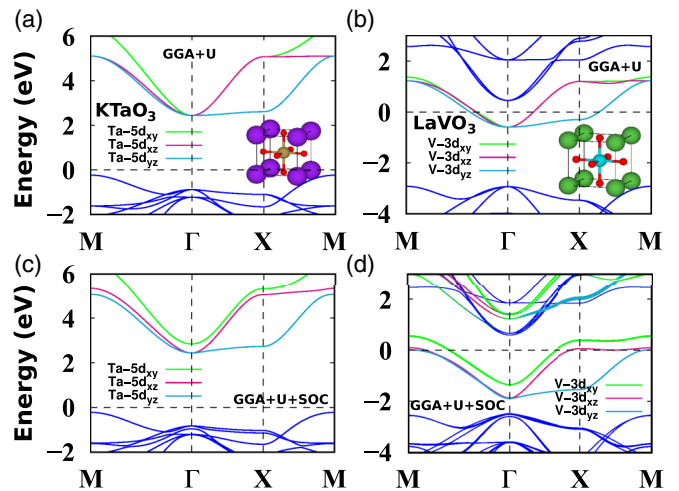


FIG. 1. GGA + U bulk band structures without SOC for the ABO_3 -type cubic perovskites of (a) KTO and (b) LVO, with corresponding crystal structures shown in the insets. The large purple (green) spheres at the corners are the A atoms, yellow (cyan) are the B atoms at the center. The oxygen atoms are shown with small red spheres. SOC-incorporated bands are shown in the bottom panel in (c) for KTO and (d) for LVO. The green, magenta, and cyan bands in all four figures present d_{xy} , d_{xz} , and d_{yz} orbitals.

The calculations are performed with a kinetic energy cut off of 530 eV, Brillouin zone sampling with a Gamma-centered $11 \times 11 \times 1$ k mesh, and energy convergence criteria of 10^{-6} eV. We fully relax the atomic positions until the force on each atom is less than 0.05 eV/Å. To discard any spurious interaction, a 20 Å vacuum is added between the periodic films. We further perform spin-polarized calculations to investigate the magnetic ground state of different combinations of LVO and KTO layers. We use the initial magnetic moment along the z direction for V sites of different layers of LVO in parallel (for ferromagnetic order) and antiparallel (for antiferromagnetic order) directions. We calculate the spin-polarized density of states using the tetrahedron smearing method as implemented in VASP.

III. CRYSTAL STRUCTURES AND INTERFACES

From our calculations we find that bulk KTO is an indirect band gap insulator with a gap ~ 2.7 eV. It is found to be in the cubic phase with space group $221 (Pm\bar{3}n)$ [see Fig. 1(a)] and lattice parameters $a = b = c = 4.03$ Å which are in good agreement with the previously reported values [18,19]. The corresponding band structure is presented in Fig. 1(a). The cubic phase of bulk LaVO_3 (LVO), on the other hand, shows metallic behavior. The calculated lattice parameter (a) of LVO is 3.95 Å in good agreement with the experimentally reported value (3.91 Å [26,27]). Naturally occurring LVO has an orthorhombic crystal structure and is an insulator with a 1.1 eV band gap [28–30]. Including SOC, we note that the degeneracy between the t_{2g} bands (d_{xy} , d_{xz} and d_{yz}) is lifted in both KTO and LVO as shown in Figs. 1(c) and 1(d), respectively. We use a cubic phase [26] of LVO for the hetero-structure with cubic KTO as a substrate to match the structures, which was most likely the case for experimental heterostructures.

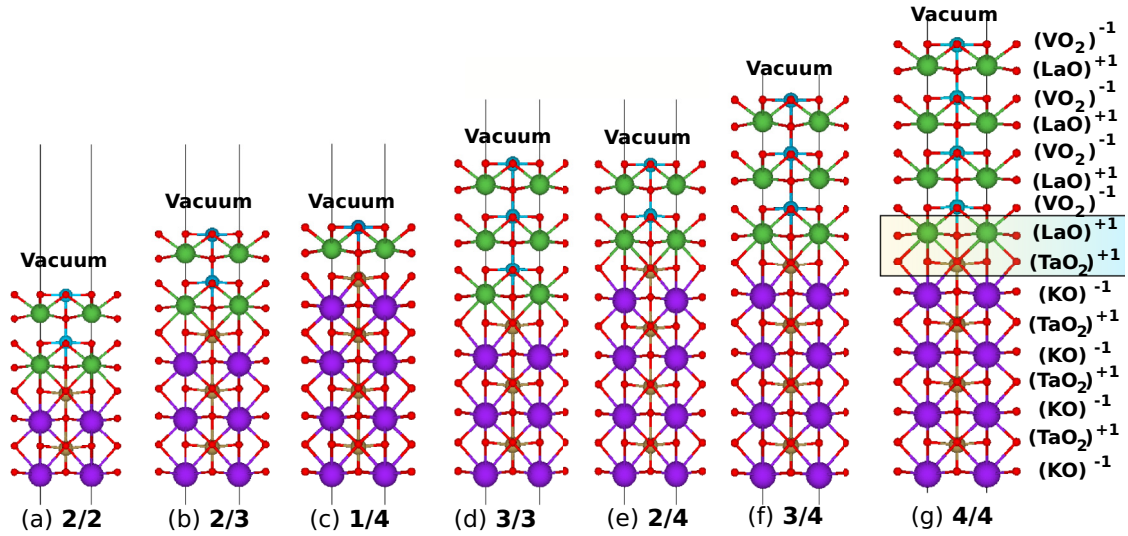


FIG. 2. [(a)–(g)] $(\text{LVO})_m/(\text{KTO})_n$ heterostructure configurations with m/n mentioned at the bottom of each. The interface is formed at the $(\text{TaO}_2)^{+1}$ termination in each configuration, shown in (g) with a shaded box. Also shown are the alternate charged layers.

To prepare the heterostructures $(\text{LVO})_m/(\text{KTO})_n$, we use different layers (m and n) of LVO and KTO. We terminate the KTO unit cell at $(\text{TaO}_2)^{+1}$ layer and LVO at $(\text{LaO})^{+1}$ layer to form a polar-polar interface, $(\text{LaO})^{+1}/(\text{TaO}_2)^{+1}$. To compare the results and see the effect of the number of layers of $(\text{LVO})_m$ and $(\text{KTO})_n$, we use various configurations as illustrated in Fig. 2. It is important to note that the crystal symmetry of the supercell structures are reduced from the bulk cubic structure to tetragonal $P4mm$ with space group No. 99. All the defined geometries are relaxed with the conjugate gradient algorithm as implemented in the VASP package. While optimizing the geometries, we kept the in-plane lattice constant equal to 4.03 \AA for all the supercells, which is also the lattice constant for bulk KTO. We are using KTO as substrate—the LVO layers are under a tensile strain of 1.98%. We check the lattice constant with the full geometry relaxation (cell parameters and atomic positions) for the smallest supercell, 2/2. The lattice constant with the fully relaxed structure for 2/2 is 3.99 \AA , that is an average of the lattice constants of LVO and KTO. In Sec. V, we will discuss in detail the difference in the electronic structures of this fully relaxed 2/2 and laterally constrained 2/2. Here we just point out that the two sets of results are in qualitative agreement.

In order to discuss the stability and possibility of the formation of the heterostructures in any given crystal structure, we calculate the formation energies for each of the configurations. The formation energy is defined as $E_{f[(\text{LVO})_m/(\text{KTO})_n]} = E_{(\text{LVO})_m/(\text{KTO})_n} - E_{(\text{LVO})_m} - E_{(\text{KTO})_n}$, where E_i are the ground state energies of the i th system. It is energetically favorable to form the heterostructures, indicated by the negative formation energies outlined in Table T1 of Ref. [44].

IV. NONMAGNETIC ELECTRONIC STRUCTURE

In the following, we perform layer-dependent electronic structure calculations for different heterostructures given in Fig. 2. We show the band structures with nonmagnetic calculations in Fig. 3. The cubic LVO being metallic, a single layer

of LVO on the KTO substrate is enough to make the interface conducting. From the nonmagnetic calculations, we observe the following.

(1) Increasing KTO layers only shifts the oxygen bands in the valence band region towards the FL but does not affect the conduction bands. The bandwidths of the systems with the same number of layers of LVO (m) are almost the same for any n , indicating the bandwidth is n -independent, where n is the number of KTO layers.

(2) Though all the surfaces under investigation are conducting, including single LVO layer, as we will discuss shortly in Sec. IV B of projected bands, more than one layer of LVO (i.e., $m > 1$) is needed for $\text{Ta}_{\text{int}} 5d_{xy}$ orbital to take part in charge transport, where Ta_{int} is the Ta atom at the interface.

(3) The interfaces with three and more than three layers of LVO (i.e., $m \geq 3$) show a Lifshitz transition [9,15] near the FL as shown in Fig. 3. It is important to mention that the Lifshitz transition is not coming from the t_{2g} manifold of the interfacial transition metal Ta. Unlike LAO/STO (Ti t_{2g} at the interface), the Lifshitz transition in the present case is formed between the interfacial Ta d_{xy} band and the V $d_{xz,yz}$ (near the interface) bands. We will have a clear idea from the projected band structure in Fig. 4 of Sec. IV B. It is well understood that the Lifshitz transition plays a vital role in anomalous transport, such as thermal conductivity, as well as the Seebeck coefficient. The change in the Fermi surface topology, induced by the Lifshitz transition, gives rise to a cusp in the dc and thermal conductivity as reported by Nandy *et al.* [15]. Our results involving multiple layers of LVO/KTO indicate that the Lifshitz transition point can be adjusted by varying the number of LVO layers, eliminating the need for external gate voltage. This feature makes these heterostructures particularly suitable for application in thermal transport devices. Among these structures, those with three layers of LVO emerge as optimal candidates due to the proximity of the Lifshitz point to the FL.

(4) Contrary to experimental claim [4], there is hardly any SOC in the bands involved in transport at the interface: the

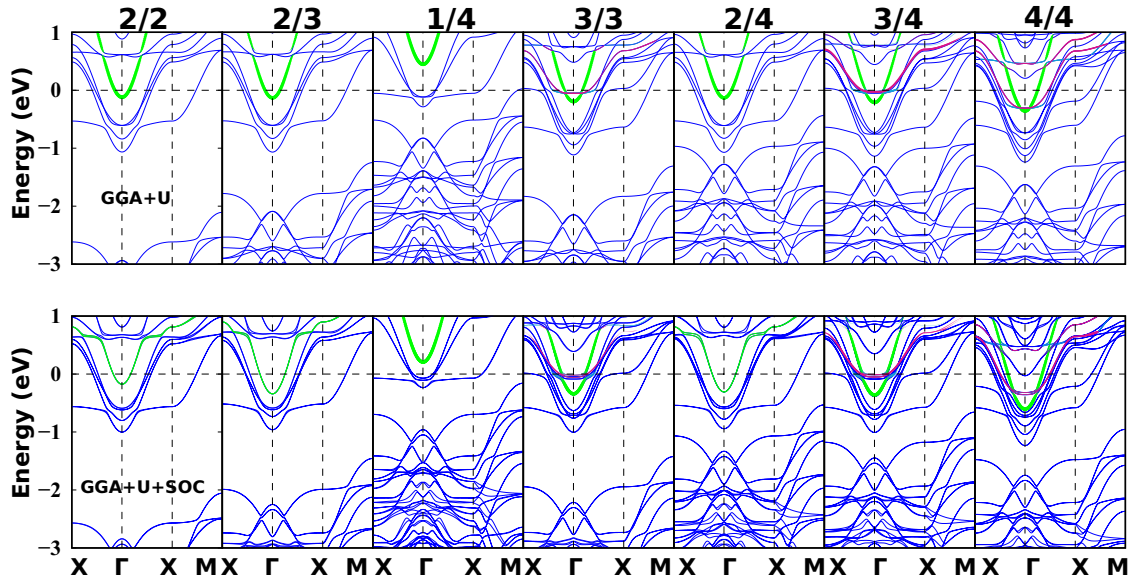


FIG. 3. Nonmagnetic band structures without (top) and with (bottom) SOC for various configurations shown in Fig. 2 along $X\text{-}\Gamma\text{-}X\text{-}M$ high symmetry path of a square Brillouin zone. The bands in green, magenta and cyan are $Ta_{\text{int}} 5d_{xy}$, $V 3d_{xz}$, and $V 3d_{yz}$, respectively. Lifshitz transition is shown for 3/3, 3/4, and 4/4 configurations with green (Ta_{int}), magenta ($V 3d_{xz}$) and cyan ($V 3d_{yz}$) bands. Both atomic and Rashba SOC are weak for all the cases. SOC breaks the degeneracy between the $3d_{xz}$ and $V 3d_{yz}$ orbitals weakly in the bands involved in the Lifshitz transition.

bands near the FL show negligible SOC. The small SOC breaks the degeneracy slightly at the Lifshitz points. The Rashba spin splitting is negligible in all the cases. Contrary to the large SOC (in the $Ta 5d$ orbitals) in bulk KTO, as shown in Fig. 1(c), the LVO/KTO interfaces studied here do not show significant SOC. A recent report, however, claims significant SOC in $\text{SrTaO}_3/\text{KTaO}_3$ interface [45] having Ta on both the materials.

A bare KTO slab was then checked for a strong Rashba spin splitting. We calculate the band structure of a thin film constructed with eight unit cells of KTO (shown in Fig. S1(a) of Ref. [44]) and find that the strength of Rashba SOC is fairly large. In Fig. S1(b) of Ref. [44], we see that there are several bands around the Γ point, with the considerable Rashba spin splitting (shown inside a red rectangle). The bands with strong Rashba spin-splittings are around 0.5 eV above the Fermi energy, while the Rashba spin-split bands for the 4/4 interface are far removed from the FL, around 1.2 eV

above it [see Figs. 3 and 4(e)]. We wish to emphasize that the spin-split bands observed in Fig. 4(e) arise from the $Ta 5d_{yz}$ and $Ta 5d_{zx}$ orbitals, and not from the $Ta 5d_{xy}$ orbital. It is probable that increasing the number of KTO layers (beyond 8) could bring these spin-split bands closer to the FL, as reported in Kakkar *et al.* [25]. The conduction band topology is unaffected with increasing number of KTO layers for the heterointerface LVO/KTO (see Fig. 3) though. It seems that the substantial Rashba spin-orbit coupling primarily originates from the KTO surface rather than the LVO layers in the LVO/KTO interfaces. Few layers of KTO have minimal Rashba SOC to show up in transport.

A. Layer projected density of states

To assess the role of individual layers within the slab, we examine the layer-projected DOS for the 4/4 LVO/KTO hetero-interface, as illustrated in Fig. S1(c) of Ref. [44]. The

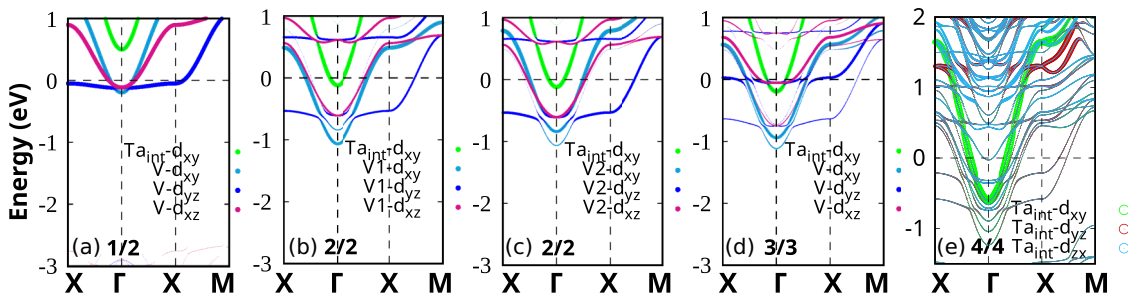


FIG. 4. The orbital-projected bands (without SOC) of $Ta_{\text{int}} 5d_{xy}$ at the interface (green), and t_{2g} of V (blue and magenta) just above the interface. V1 and V2 in (b) and (c) represent the nearest and farthest V atoms from the interface, respectively. (d) The bands shown in green, blue and magenta circles participate in the Lifshitz transition near the FL in a 3/3 interface. (e) The projected bands with SOC for 4/4 case. The Rashba spin-split bands, contributed by $Ta d_{yz,zx}$, are about 1.2 eV above the FL.

layer-projected DOS analysis reveals that, among all the Ta atoms in the KTO substrate, only the interfacial Ta atom (Ta_{int}) participates in charge transport. Conversely, all the V atoms in the slab contribute to the FL. Our layer-projected DOS highlights a nearly equal contribution from all V atoms at the FL.

B. Projected band structure

To gain insight into the distinct orbital contributions at the interface, we illustrate orbital-projected bands without SOC in Fig. 4. Figure 4(a) reveals that, in the context of $1/n$ (one layer of LVO and n layers of KTO), only the t_{2g} band manifold of V $3d$ bands is contributing near the FL, with the interfacial Ta playing no role in transport. The green band is the d_{xy} orbital of the interfacial Ta atom. Our analysis indicates that more than one layer of cubic LVO is necessary to bring the interfacial Ta $5d_{xy}$ band down to the FL. For the $2/2$ configuration [refer to Figs. 4(b) and 4(c)], both the $d_{xz,yz}$ bands from the nearest and farthest V atoms contribute nearly equally. As previously noted, the Lifshitz transition is evident in cases involving three or more layers of LVO, as shown in Fig. 4(d), where a Lifshitz transition occurs between Ta_{int} d_{xy} and V $d_{xz,yz}$ bands. Here, the interfaces with three layers of LVO are intriguing due to their Lifshitz point being closest to the FL, as observed in Fig. 4(d). This characteristic, presumably, makes the $3/n$ heterostructures ideal candidates for thermoelectric applications. The Rashba spin-split bands for the $4/4$ system are depicted in Fig. 4(e) with red and blue circles. It is important to reiterate that the Rashba spin-splitting in the Ta d_{xy} band is minimal, while a significant contribution to Rashba SOC strength is observed in the Ta $d_{yz,zx}$ bands approximately 1.2 eV above the FL.

C. Model Hamiltonian

To conduct a theoretical analysis of physics near the Lifshitz point, we formulate an effective Hamiltonian model. In the absence of SOC, we specifically select three bands in close proximity to the Fermi energy [refer to Fig. 4(d)]. These bands originate from the contributions of Ta d_{xy} and V $d_{xz,yz}$. The corresponding Hamiltonian model for these three bands is expressed through Slater-Koster integrals, defined as follows.

$$\begin{aligned} t_{xy,xy} &= 3m^2n^2t_{dd\sigma} + (m^2 + n^2 - 4m^2n^2)t_{dd\pi} \\ &\quad + (l^2 + m^2n^2)t_{dd\delta}, \\ t_{yz,yz} &= 3l^2m^2t_{dd\sigma} + (l^2 + m^2 - 4l^2m^2)t_{dd\pi} \\ &\quad + (n^2 + l^2m^2)t_{dd\delta}, \\ t_{zx,zx} &= 3n^2l^2t_{dd\sigma} + (n^2 + l^2 - 4n^2l^2)t_{dd\pi} \\ &\quad + (m^2 + n^2l^2)t_{dd\delta}, \end{aligned} \quad (1)$$

where l , m , and n are the direction cosines of Ta atom at the interface and V atom near the interface, and $t_{dd\sigma}$, $t_{dd\pi}$, and $t_{dd\delta}$ are the Slater-Koster overlap parameters.

We construct the three-band model Hamiltonian,

$$\mathcal{H}_0 = \begin{pmatrix} h_1 & h_{12} & h_{13} \\ h_{21} & h_2 & h_{23} \\ h_{31} & h_{32} & h_3 \end{pmatrix} = \begin{pmatrix} h_1 & 0 & 0 \\ 0 & h_2 & 0 \\ 0 & 0 & h_3 \end{pmatrix} \quad (2)$$

with h_1 , h_2 , and h_3 being d_{xy} , d_{yz} , and d_{zx} band dispersion relations, respectively. The off-diagonal elements are zero due to symmetry of the orthogonal orbitals. These diagonal matrix elements are constructed using the Slater-Koster integrals as we present in Eq. (3).

$$\begin{aligned} h_1 &= \epsilon_1 - 2t_1(\cos(k_x) + \cos(k_y)) - t_2 - 4t_3 \cos(k_x) \cos(k_y), \\ h_2 &= \epsilon_2 - 2(t_1 \cos(k_x) + t_2 \cos(k_y)) - t_1 - 2t_3 \cos(k_y), \\ h_3 &= \epsilon_3 - 2(t_2 \cos(k_x) + t_4 \cos(k_y)) - t_4 - 2t_5 \cos(k_x), \end{aligned} \quad (3)$$

where ϵ_i are the onsite energies for Ta d_{xy} and V $d_{xz,yz}$ orbitals, and t_i 's are the hopping integrals. The t_{2g} bands around Γ point are present in Fig. S2 of Ref. [44]. The strong hybridization between three orbitals leads to avoided band crossings around the Γ point. This avoided crossing also represents a broken symmetry which is the inversion symmetry in the case of the interface. We incorporate the broken inversion symmetry in the tight-binding Hamiltonian using atomic SOC and the orbital Rashba effect. The atomic SOC and the orbital Rashba Hamiltonian, in basis of $[\text{Ta } d_{xy,\sigma}, \text{V } d_{yz,\sigma}, \text{V } d_{zx,\sigma}]$, σ is the spin index, can be defined in the following manner [10]:

$$\mathcal{H}_{\text{ASO}} = \frac{\zeta}{2} \begin{pmatrix} 0 & 0 & 0 & 0 & 1 & -i \\ 0 & 0 & i & -1 & 0 & 0 \\ 0 & -i & 0 & i & 0 & 0 \\ 0 & -1 & -i & 0 & 0 & 0 \\ 1 & 0 & 0 & 0 & 0 & -i \\ i & 0 & 0 & 0 & i & 0 \end{pmatrix}, \quad (4)$$

$$\mathcal{H}_{\text{RSO}} = \gamma \begin{pmatrix} 0 & -2i \sin(k_x) & -2i \sin(k_y) \\ 2i \sin(k_x) & 0 & 0 \\ 2i \sin(k_y) & 0 & 0 \end{pmatrix}, \quad (5)$$

where ζ and γ are the atomic and Rashba SOC, respectively. The effective Hamiltonian including spin-orbit interactions is $\mathcal{H} = \mathcal{H}_0 + \mathcal{H}_{\text{ASO}} + \mathcal{H}_{\text{RSO}}$. Fitting this six-band Hamiltonian near the Γ point gives us the unknown parameters, which are as follows (in eV): $\epsilon_1 = 0.76$, $\epsilon_2 = 0.7$, $\epsilon_3 = 0.57$, $t_1 = 0.0919$, $t_2 = 0.1778$, $t_3 = 0.2048$, $t_4 = 0.1186$, $t_5 = 0.1295$, $\zeta = 0.03$, and $\gamma = 0.015$. The fitted bands using these parameters are presented in Fig. S2 of Ref. [44].

In Fig. 5, we depict the Fermi surface, illustrating its transformation under varying chemical potentials (μ). The Lifshitz transition, denoting a shift in the Fermi surface topology, can be controlled experimentally by adjusting the chemical potential, carrier density, and, consequently, the Lifshitz point through gate voltage modulation. Notably, at $\mu = -0.42$ eV, only two orbitals form electron-like pockets, but as μ increases, additional electron-like pockets emerge as shown in Fig. 5. At $\mu = -0.33$ eV, all three pockets contribute to the Fermi surface. This highlights the $3/3$ configured hetero-interface as an optimal choice for transport devices due to its proximity to the FL.

V. MAGNETIC ORDERING

Numerous investigations are available in literature for the magnetic characteristics of bulk LVO compound [28,46–49].

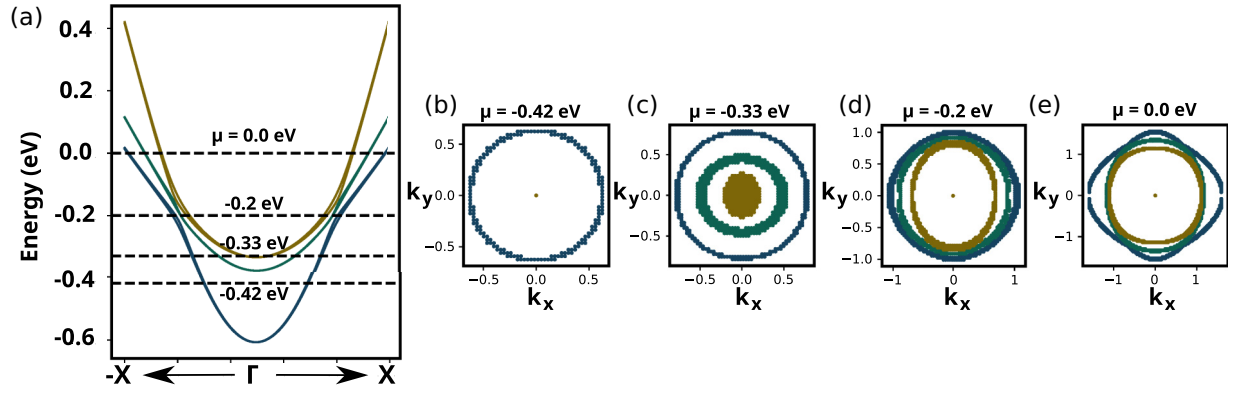


FIG. 5. (a) The tight-binding band structure and [(b)–(e)] the change in the Fermi surface topologies can be observed at different chemical potentials (μ). The Fermi surfaces are plotted in the k_x - k_y plane and in units of π .

With a total spin moment $S = 1$ from V^{3+} ionic configuration ($3d^2$), vanadium (V) plays a crucial role in the magnetism of LVO. The pseudo-cubic phase of LVO, with a tetragonal distortion of the cubic structure, exhibits C-type antiferromagnetic (AFM) order at low temperatures. In the C-type AFM, V moments in the basal plane (ab plane) are antiferromagnetically ordered while the moments along the c axis are ordered ferromagnetically. The susceptibility displays a peak at the transition temperature $T_N \sim 140$ K and there is a concomitant orthorhombic to monoclinic transition at that temperature [28,49]. Conversely, the cubic LVO, sharing the same space group as KTO ($Pm\bar{3}n$), is claimed to be ferromagnetic (FM) [32]. In Fig. 6(a), we present the spin-polarized DOS for bulk cubic LVO, revealing the unmistakable FM nature of the cubic phase. Notably, the DOS illustrates a substantial band gap (approximately 4 eV) in the spin-down channel, while the spin up channel shows finite DOS at FL, indicative of a *half-metal*. This was reported earlier as well [32]. The *half-metallic* character, a distinctive feature of the ferromagnetic state [50], has its potential utility in spintronics devices, where both spin current and charge current are harnessed [51–56].

To explore the magnetic order in the (001) interface composed of LVO/KTO, we conducted spin-polarized density functional theory calculations for a range of interfaces illustrated in Fig. 2. The sublattice magnetization was constrained to exhibit parallel alignment on V atoms across different layers for FM order and antiparallel alignment for AFM order. The crystal structures are relaxed with different magnetic orderings, by keeping again the in-plane lattice constant fixed. The relaxed geometries are shown in Fig. S3(b) of Ref. [44]. After relaxation there is a uniform elongation of the atomic layers in the magnetic case, making the system more stable compared to the nonmagnetic case (Fig. S3(a) of Ref. [44]), where the LVO and KTO layers are nonuniformly deforming the overall geometry. This uniform relaxation of atomic positions in the magnetic case is possibly the reason for the insulating phases, which we are going to discuss shortly. Moreover, we also perform a full geometry relaxation (atomic positions and lattice parameters), and find that the electronic structure of the system is unaltered, implying the local relaxations are more important than the global geometry relaxation. The AFM DOS for 2/2 with partial (atomic positions) and

full geometry relaxation are shown in Fig. S4 of Ref. [44]. We then compared the spin-polarized ground state energies (GSEs) of all the heterostructures, considering various magnetic orderings such as nonmagnetic (NM) with zero moment, FM, and AFM. By AFM we mean that each V layer is ferromagnetic but the layers are antiferromagnetically ordered as one goes from one layer to the next in the (001) direction. In a bulk system this type of AFM ordering is referred to as A-AFM. The resulting data are organized in Table I. Notably, we observe that energetically the AFM ground state consistently emerges as the most favorable ground state in all the heterostructures excepting for the monolayer of LVO. An

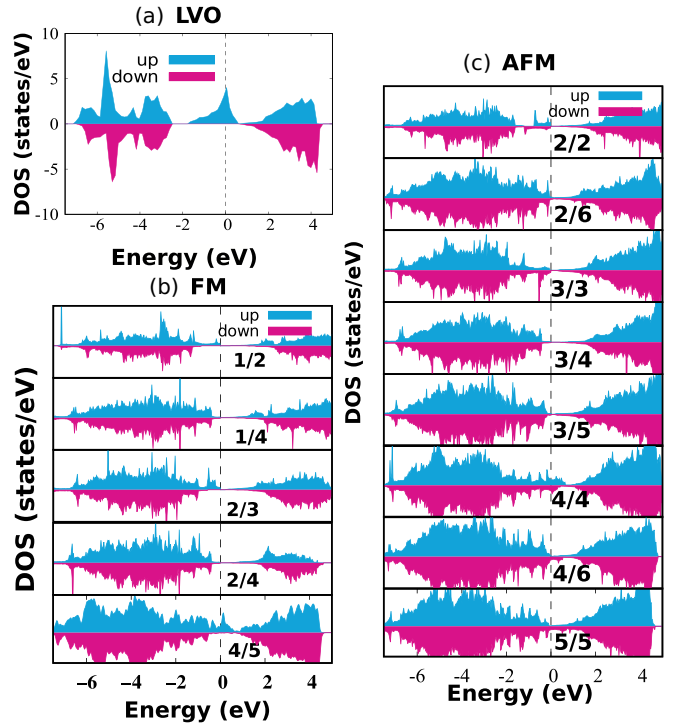


FIG. 6. (a) The spin-resolved density of states (DOS) for the cubic LVO. The gap in the minority spin channel shows it is an FM *half-metal*. (b) The FM DOS for various interfaces. (c) DOS for the AFM order. The DOS range for all the plots is -20 to 25 states/eV.

TABLE I. The ground state energies (in eV) for nonmagnetic (NM), ferromagnetic (FM), and antiferromagnetic (AFM) ordering. FM implies both intraplanar (parallel to the interface) and interplanar (perpendicular to the interface) spin orientations, and AFM implies intraplanar ordering is ferromagnetic and interplanar nearest-neighbor ordering is antiferromagnetic (commonly known as A-AFM in 3D magnetically ordered systems). The value of U used for V $3d$ orbitals is 3 eV (the cases with $U = 5$ eV are shown in the bracket).

interface	NM (eV)	FM (eV)	AFM (eV)	Nature
1/2	-112.212	-113.655		FM-Insulator
1/4	-186.148	-187.592		FM-Insulator
2/2	-151.557	-153.938 (-151.952)	-153.989 (-151.985)	AFM-Insulator
2/3	-188.520	-190.907	-190.959	AFM-Insulator
2/4	-225.475	-227.868	-227.923	AFM-Insulator
2/6	-299.447	-301.853	-301.896	AFM-Insulator
3/3	-227.694	-230.728	-231.187	AFM-Insulator
3/4	-264.643	-266.855 (-264.568)	-267.794 (-265.085)	AFM-Insulator
3/5	-301.649	-304.962	-305.166	AFM-Insulator
4/4	-303.897	-307.732	-308.364	AFM-Metal
4/5	-340.926	-345.012	-345.082	AFM-Metal
4/6	-375.535	-380.743	-382.245	AFM-Metal
5/5	-380.247	-385.253	-385.732	AFM-Metal

examination of Table I reveals a small difference (approximately 0.1 eV) between GSEs of FM and AFM with equal number of LVO and KTO layers, suggestive of a potential coexistence of AFM and FM ground states [57], and a possible transition between them. To assess the stability of the magnetic behavior with variations of Hubbard U , we perform the spin-polarized calculations for some of the interfaces with a higher U of 5 eV. Assuredly, the ground state remains nearly insensitive to changes in U , as evidenced by the GSEs detailed in Table I.

As we noted earlier in the introduction, the local symmetries of bulk materials could be lowered by forming heterostructures resulting in MIT [23,24]. If the energy can be lowered by lowering symmetries, it indicates a possible stable phase and an electronic phase transition might occur. By forming interfaces and introducing magnetic order, we break crystal symmetries. We calculated the relative GSEs per formula unit for each configuration and found that the energies are lowered for magnetic states. The measured relative GSEs are tabulated in Table T2 of Ref. [44]. We find that the AFM and FM are more stable than the nonmagnetic phases. However, even though we have symmetry breaking in the system, it is not enough to open a gap at the FL in the single particle spectrum. In order to open a band gap, addition of Hubbard- U in the density functional calculations is required (in addition to local structural and magnetic SBs). For example, we check the AFM-DOS without and with U for the 2/2 LVO/KTO heterostructure (see Fig. S5 of Ref. [44]), and find that effect of electron-electron correlation is necessary for a gap to open up between occupied and unoccupied single particle states.

Examining the ferromagnetic DOS (though it is less stable compared to AFM) shown in Fig. 6(b), it is evident that the interfaces exhibit a *half-metallic* behavior. Specifically, only one spin channel conducts at the FL, while the other channel remains gapped. All FM LVO/KTO (001) interfaces appear to possess inherent *half-metallic* character beyond three LVO layers. It is crucial to highlight that the bulk LVO itself is *half-metallic*, but this *half-metallicity* is suppressed in $(\text{LVO})_m/(\text{KTO})_n$ heterostructures, where, $m < 4$. In these cases, the system makes a transition to an insulating state. It

requires more than three layers of LVO for the bands of one of the spin channels to appear at the FL in the FM heterostructure, and make it conducting (as *half-metal*). This is illustrated in Fig. 6(b). Turning attention to the AFM cases in Fig. 6(c), it is seen that they exhibit insulating behavior for configurations with fewer than four layers of LVO. Additionally, the magnetic moment on each V atom is found to be slightly less than $2\mu_B$.

In order to understand the underlying mechanism for the magnetic ordering, we plot the orbital levels and corresponding orbital-projected, spin-resolved density of states in Fig. 7 of different interfaces with different magnetic and conducting characters. Also shown are the primary location of the two electrons of V^{3+} in its outermost shell. Analyzing the spin-resolved DOS as presented in Fig. 6, we identified different magnetic characteristics for configurations 2/2, 2/4, 4/4, and 4/5, classifying them as FM-insulator, FM-*half-metal*, AFM-metal, and FM-*half-metal*, respectively. We report for all possible conducting and magnetic orderings for the sake of completeness, even though the interlayer AFM is the most stable phase. The Goodenough-Kanamori-Anderson (GKA) rule [58–62] may be used to interpret the magnetic behavior of the 2/2 configuration shown in Fig. 7(a). In the 2/2 heterostructure, antiferromagnetic coupling along the c axis arises from a superexchange mechanism facilitated by oxygen anions. This can be seen from the DOS plot shown in Fig. S6 of Ref. [44], where oxygen and V atom-projected DOS are present on the same energies just below the FL. This involves a virtual hop between the two V^{3+} ions via the intervening oxygen. Specifically, the superexchange involves a p - d hopping process where O $2p$ orbitals overlap with V $3d_{xz,yz}$ orbitals. Moreover, the σ overlap of $2p$ orbitals with the e_g orbitals is stronger than the π overlap with the t_{2g} orbitals, indicating a relatively weak antiferromagnetic superexchange in the case of the 2/2 interface. The DOS in Fig. 7(b) is essential to understand the ferromagnetic exchange in 2/4. Here, both V1 and V2 exhibit the same spin-orbital order, featuring a gap where the FL is elevated compared to 2/2. The FM superexchange mechanism governs the behavior of the 2/4 FM insulator, wherein an occupied and an empty

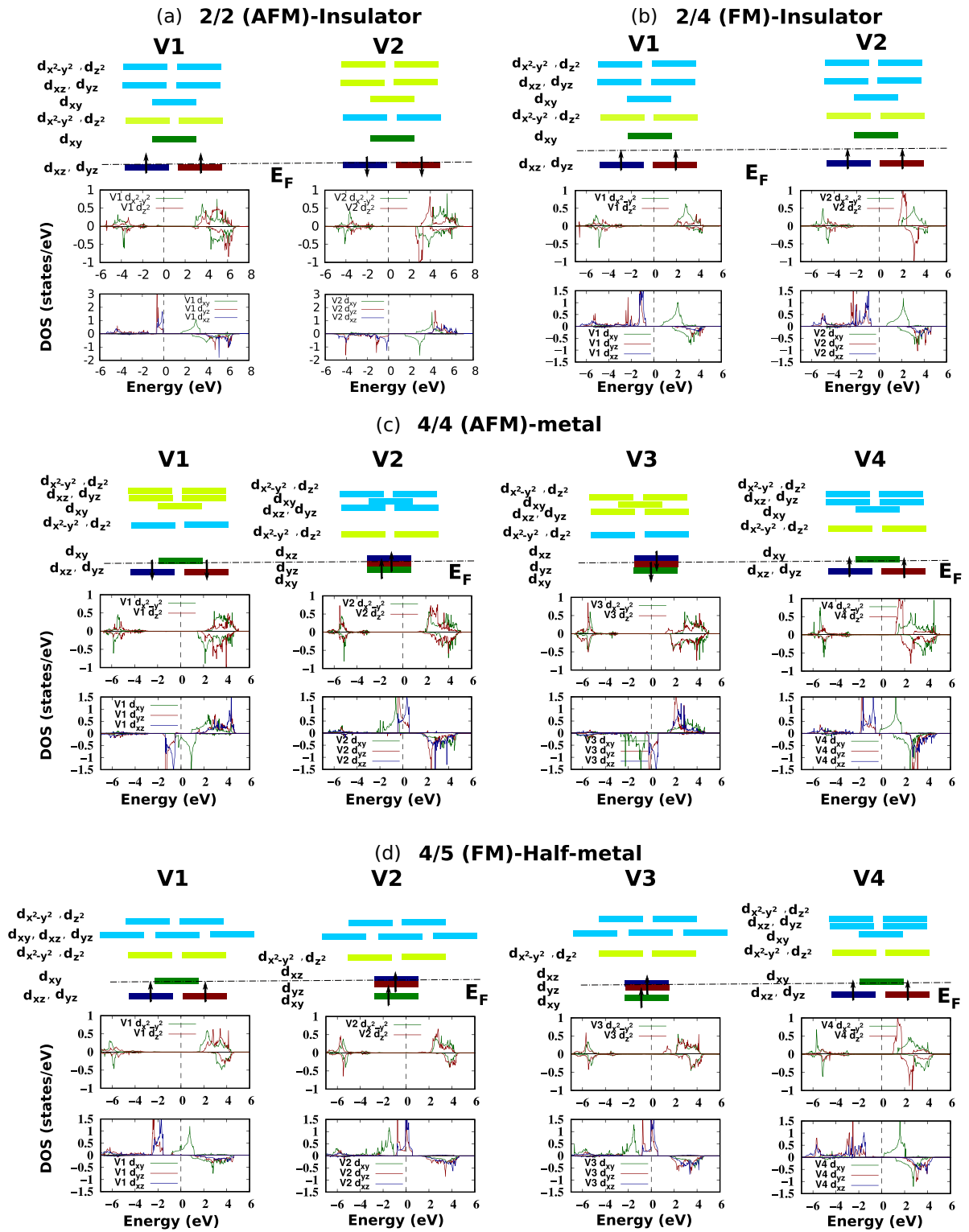


FIG. 7. The orbital occupations with spin-levels shown in light green (spin-up) and cyan (spin-down) for (a) 2/2, (b) 2/4, (c) 4/4, and (d) 4/5 interfaces. V1, V2, etc. are the vanadium ions (V^{3+}). The vanadium ion nearest to the interface is V1. Black dashed lines are the Fermi levels in all cases. Corresponding orbital-projected spin-resolved DOS are shown in the lower panels: e_g and t_{2g} orbitals in the middle and lower panels, respectively.

orbital exchange electrons via oxygen. This superexchange is relatively weak in the 2/4 scenario, as the t_{2g} orbitals bond with O $2p$ orbitals through π overlap.

Next we analyze the DOS for the 4/4 interface where insulator-metal transition occurs [shown in Fig. 7(c)]. Clearly, t_{2g} orbitals are dominantly taking part at the FL. Focusing on

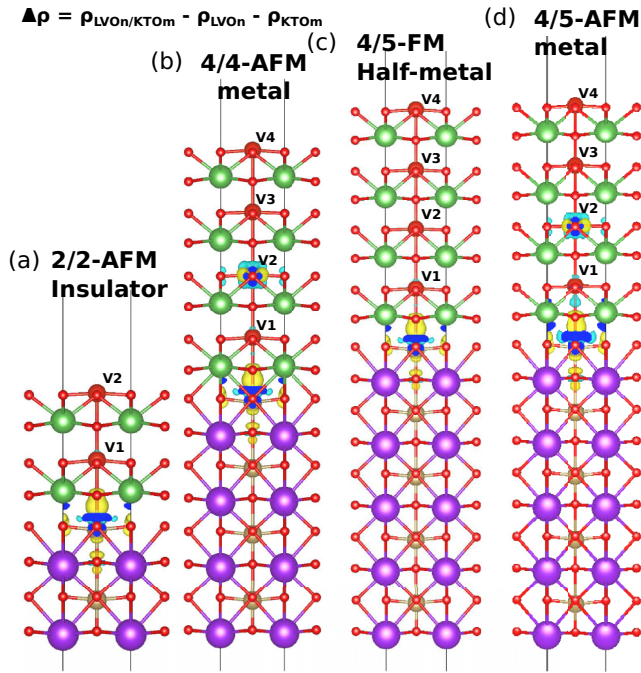


FIG. 8. The charge density difference ($\Delta\rho$) plots for (a) 2/2, AFM-insulator, (b) 4/4, AFM-metal, (c) 4/5, FM-half-metal, and (d) 4/5, AFM-metal. Yellow surfaces represent electron clouds and the blue regions represent electron depletion. The isosurface value is set at $0.005 e/\text{\AA}^3$.

a particular orbital, such as d_{xy} (indicated by the green lines in the lower panels of Fig. 7(c)), of V1 and V2, they touch each other just below the FL with their opposite spin moments. The same is true for V3 and V4 as shown in the last two panels of Fig. 7(c). In this scenario, electrons hop between nearest V^{3+} ions along the c axis via intervening oxygen leading to interplanar antiferromagnetic superexchange. A direct exchange mechanism can be utilized to explain the FM half-metal character in 4/5, with no contribution from down spins from any of the V atoms. It is important to remark that in the 4/4 and 4/5 configurations of Figs. 7(c) and 7(d), the inner V^{3+} ions (V2 and V3) are alike in terms of DOS, while the outermost V^{3+} ion (V4) is similar to the one near the interface (V1). This suggests there is an interaction which connects interface to the surface, such as electron reconstruction mechanism.

The AFM-metallic phases are always intriguing. In order to get insights how AFM-metallic phases of $4/n$ interfaces are different from AFM-insulator (2/2) and FM-half-metals, and understanding the charge reconstruction mechanism, we plot the charge density difference in Fig. 8. One thing which is common in all the four cases is the formation of two-dimensional electron gas (2DEG) at the interface. This indicates charge accumulation at the interfacial Ta_{int} , as will be further demonstrated by the partial free charge carriers we will discuss shortly. The formation of the interface attracts charges from the surface and bulk layers and induce electronic interactions at the interface of both the materials leading to conduction of the interface. The only difference among all is observed in the $4/n$ cases [see Figs. 8(b) and 8(d)], where it is clearly seen that there are more charge accumulation at

the V2 site. As we mentioned earlier, $4/n$ is the case where the AFM interfaces start conducting and showing a transition from insulating to metallic phase. We see that there is a charge leftover at V2 after subtracting the charge densities of LVO and KTO, and this leftover charge is supposed to be the source of the metallic AFM phase in the $4/n$ interfaces. We also calculate partial free charge carrier stemming from different V atoms by integrating the atom-projected DOS near the FL for the 4/4 interface (shown in Fig. S9 of Ref. [44]). There are mixed charge carriers (electrons and holes) at the interface whose magnitudes are given in Table T3 of Ref. [44]. We find that holes are in majority, which are contributed by the internal V atoms, V2 and V3. There is a small contribution of electrons at Ta_{int} (see Table T3 of Ref. [44]).

We will now discuss the electronic polarization originated from the polar distortions in the insulating interfaces using Berry phase method [63–65]. Our focus lies specifically on the aggregate electronic polarization within magnetic insulating interfaces. A comprehensive examination of local polarizations and their associated distortions necessitates a separate, detailed investigation. The total electronic polarization calculated for 2/2-AFM, 2/3-AFM, and 3/3-AFM insulating interfaces are 0.24 , 0.71 , and 0.73 C/m^2 , respectively. It is crucial to underscore that the relaxation of crystal geometries induces local distortions, resulting in a charge imbalance and the formation of dipoles. These dipoles constitute the primary origin of electronic polarization within the system. In contrast, the unrelaxed geometries exhibit have higher energy, are metallic, and do not support dipole moments.

In the oxide interfaces of this nature, as highlighted in our introduction, achieving a critical thickness is pivotal for metallicity of the interface. Contrary to experimental claims [4] our study emphasizes the consideration of magnetic interactions for the determination of the critical thickness and there is no unique value for every m/n combination. Our spin-polarized calculations demonstrate that, for the interface to exhibit conductivity, a critical thickness of no less than four layers of LVO, featuring interplanar AFM interactions, is imperative (Fig. 6).

VI. $\sqrt{2} \times \sqrt{2}$ SUPERCELLS

To explore the intra and interlayer magnetic coupling further and to confirm that intra-planar exchange between V moments is ferromagnetic, we construct a $\sqrt{2} \times \sqrt{2}$ supercell for the 2/2, 3/3 and 4/4 supercells. We expand the 1×1 supercells along the diagonal direction, the in-plane lattice constant of the new supercells is now $\sqrt{2}a = 5.70 \text{ \AA}$ (a is the lattice constant of 1×1 supercell). Therefore the new supercells have two transition-metal (TM) ions within each plane. In the $\sqrt{2} \times \sqrt{2}$ supercells, there are two magnetic V^{3+} ions in each plane, one at the corner (V1) and another at the center (V2), the schematic of which is shown in Fig. 9(a). A relaxed structure is also shown in Fig. S8 of Ref. [44] for the 3/3 heterostructure. All the atomic positions and the lattice geometries are allowed to relax and buckling in the bonds can be seen after the relaxation. The La-O and V-O (K-O and Ta-O) bonds bend in the downward (upward) direction along the c axis and the overall bond angle (O-M-O, where M is A or B of the ABO_3 complex) in the plane deviates from 180° .

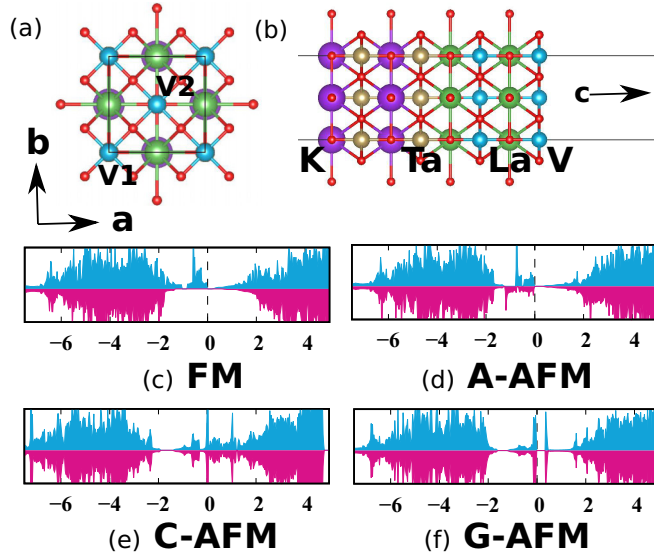


FIG. 9. (a) Top and (b) side views of a $\sqrt{2} \times \sqrt{2}$ supercell for the 2/2 configuration. V1 and V2 indicate the magnetic V^{3+} ions at the corner and at the center of the supercell, respectively. There are four magnetic ions in this 2/2 supercell, two in each layer, posing a possibility for FM, A-AFM, C-AFM, and G-AFM. Respective spin-polarized DOSs are shown in (c) FM, (d) A-AFM, (e) C-AFM, and (f) G-AFM. Vacuum is added along the c direction as shown by the arrow in (b).

As discussed for the normal supercells, the $\sqrt{2} \times \sqrt{2}$ supercells also show an overall elongation along the c axis. LVO and KTO layers stretch in the opposite directions inducing a polar distortion between LVO and KTO (see Fig. S8(b) of Ref. [44]). The $\sqrt{2} \times \sqrt{2}$ supercells make it possible to study various AFM orders, such as A-AFM, C-AFM and G-AFM. In the A-AFM, all the magnetic ions in a plane are aligned along the z direction while the ones in the next plane are oppositely aligned. In C-AFM order, the spins of the corner ions are up in each layer while the spins at the central atoms are down. In G-AFM, all the nearest-neighbor spins are aligned opposite to each other. Comparing the GSEs for the normal 1×1 and the $\sqrt{2} \times \sqrt{2}$ supercells, for FM and A-AFM order, we note that the GSEs are exactly doubled due to doubling of the system size, within the accuracy of ~ 0.01 eV. We next calculate the GSEs for all the four (FM, A-AFM, C-AFM, and G-AFM) magnetic orders, and find that the A-AFM is the most stable state and the FM is the second most stable, except

TABLE II. The ground state energies per unit cell (in eV) for ferromagnetic (FM), A-type antiferromagnetic (A-AFM), C-AFM, and G-AFM orderings for $\sqrt{2} \times \sqrt{2}$ supercells. The GSEs suggest that the A-AFM is the most stable and the FM is the second most stable state, except 1/ n .

interface	FM	A-AFM	C-AFM	G-AFM	Nature
1/2	-227.326		-227.413		AFM-Insulator
1/4	-375.194		-372.613		FM-Insulator
2/2	-307.876	-307.985	-305.313	-306.408	A-AFM-Insulator
3/3	-462.285	-462.462	-459.698	-461.020	A-AFM-Insulator
4/4	-616.250	-616.591	-613.942	-616.337	A-AFM-Metal

1/2 and 1/4- $\sqrt{2} \times \sqrt{2}$ supercells. In 1/2, the intralayer AFM is more stable as compared to intralayer FM. The intralayer AFM in 1/2 is slightly lower in energy (0.08 eV) as compared to the FM. On the other hand, the trend in 1/4 is consistent with other m/m configurations (shown in Table II) for which the intralayer AFM is the less stable as compared to the intralayer FM. The C-AFM magnetic state possesses highest GSE, implying that 2D antiferromagnetism (in a single plane) is unstable. Our study thus suggests that the interlayer AFM coupling (A-AFM) is favorable and the intralayer coupling is ferromagnetic (as against C and G-type AFM). Therefore, the stable AFM orders are, in fact, A-type AFM ground states. We plot the corresponding DOS in Figs. 9(c)–9(f). We notice that the FM and A-AFM are insulating with the valence bands almost touching but not crossing the FL. We also show that the DOS for the normal 2/2 supercell are insulating for the FM and the A-AFM states (Fig. 6). The DOS for 1/2, 1/4, 3/3 and 4/4- $\sqrt{2} \times \sqrt{2}$ supercells are shown in Fig. S7 of the Ref. [44]. 1/2 and 1/4 are insulating in their stable phases, intralayer AFM and FM, respectively. For 3/3 and 4/4, the A-type AFM is the most stable state with insulating and metallic property, respectively, as shown in Figs. S7(i) and S7(n). Thus, we find that the critical thickness for metallicity of LVO/KTO heterostructures is more than three layers of LVO, that holds true even for the extended $\sqrt{2} \times \sqrt{2}$ supercells. In addition, magnetism plays an important role in confirming the experimentally observed insulator to metal transition.

VII. DISCUSSION AND CONCLUSIONS

In summary, we studied several heterostructures formed out of cubic LVO and KTO perovskites, stacked along the (001) direction. We assessed their stability by computing their formation energies, with negative values indicating the feasibility of interfaces with cubic KTO as the substrate, despite LVO naturally existing in the orthorhombic phase. We study both nonmagnetic and magnetic cases. Our findings for the nonmagnetic case are as follows. (1) To have Ta $5d_{xy}$ states participate in transport, a minimum of two cubic LVO layers is necessary. (2) Mostly, t_{2g} bands of all the $3d$ -V atoms contribute to the FL, while only Ta_{int} $5d_{xy}$ band plays any role. (3) The Lifshitz transition, observed in interfaces with three or more layers of LVO, involves V $3d_{xz,yz}$ bands near the interface and Ta $5d_{xy}$ at the interface, in contrast with LAO/STO interface, where the transition occurs among the t_{2g} bands of Ti at the interface. This underscores the intricate

multiatom multi-orbital contributions to the transport phenomenon in these heterostructures. Furthermore, our study demonstrates that the bands involved in the Lifshitz transition can be finely tuned using the thickness of LVO and KTO. (4) Notably, our band structure and the model Hamiltonian study predicts negligible Rashba SOC, raising questions about the significance of SOC in transport. Additional layers of KTO, while keeping LVO layers constant, have minimal effects on the physics near the FL.

Magnetism in LVO/KTO heterostructures, is primarily influenced by the magnetic properties of LVO. Spin-polarized DFT calculations indicate that in LVO/KTO heterostructures, the interlayer AFM ordering, commonly known as A-AFM, ground state is the most favorable, while the nonmagnetic ground state being the least stable. We observe that if the number of LVO layers are fewer than four, the A-AFM ground states become insulating. The DOS for ferromagnetic heterostructures demonstrates a *half-metallic* character. The small energy difference between FM and AFM ground state energies implies a potential coexistence of AFM and FM ground states. Superexchange interaction mediated via oxygen ions is responsible for the antiferromagnetic coupling, while a direct exchange most likely leads to ferromagnetic coupling. The magnetic interactions are necessary to explain

the critical thickness of LVO for the conducting LVO/KTO heterostructures. The extended $\sqrt{2} \times \sqrt{2}$ supercells further confirms the essential role of magnetic interactions in elucidating the critical thickness of LVO. Furthermore, it is also shown that A-AFM (interlayer AFM and intralayer FM) is most stable state for all m/n , except $1/2$, for which the intralayer AFM is favorable.

ACKNOWLEDGMENTS

We acknowledge National Supercomputing Mission (NSM) for providing computing resources of “PARAM Shakti” at IIT Kharagpur, which is implemented by C-DAC and supported by the Ministry of Electronics and Information Technology (MeitY) and Department of Science and Technology (DST), Government of India. The work at Los Alamos National Laboratory was carried out under the auspices of the U.S. Department of Energy (DOE) National Nuclear Security Administration under Contract No. 89233218CNA000001. It was supported by the LANL LDRD Program, and in part by the Center for Integrated Nanotechnologies, a DOE BES user facility, in partnership with the LANL Institutional Computing Program for computational resources.

-
- [1] A. Ohtomo and H. Hwang, A high-mobility electron gas at the LaAlO₃/SrTiO₃ heterointerface, *Nature (London)* **427**, 423 (2004).
- [2] A. D. Caviglia, S. Gariglio, C. Cancellieri, B. ac  p  , A. Fete, N. Reyren, M. Gabay, A. F. Morpurgo, and J.-M. Triscone, Two-dimensional quantum oscillations of the conductance at LaAlO₃/SrTiO₃ interfaces, *Phys. Rev. Lett.* **105**, 236802 (2010).
- [3] J. A. Bert, B. Kalisky, C. Bell, M. Kim, Y. Hikita, H. Y. Hwang, and K. A. Moler, Direct imaging of the coexistence of ferromagnetism and superconductivity at the LaAlO₃/SrTiO₃ interface, *Nat. Phys.* **7**, 767 (2011).
- [4] N. Wadehra, R. Tomar, R. M. Varma, R. Gopal, Y. Singh, S. Dattagupta, and S. Chakraverty, Planar hall effect and anisotropic magnetoresistance in polar-polar interface of LaVO₃-KTaO₃ with strong spin-orbit coupling, *Nat. Commun.* **11**, 874 (2020).
- [5] Y. Wang, W. Tang, J. Cheng, M. Behtash, and K. Yang, Creating two-dimensional electron gas in polar/polar perovskite oxide heterostructures: first-principles characterization of LaAlO₃/A⁺B⁵⁺O₃, *ACS Appl. Mater. Interfaces* **8**, 13659 (2016).
- [6] S. Thiel, G. Hammerl, A. Schmehl, C. W. Schneider, and J. Mannhart, Tunable quasi-two-dimensional electron gases in oxide heterostructures, *Science* **313**, 1942 (2006).
- [7] R. Pentcheva and W. E. Pickett, Avoiding the polarization catastrophe in LaAlO₃ overlayers on SrTiO₃(001) through polar distortion, *Phys. Rev. Lett.* **102**, 107602 (2009).
- [8] J. Zhou, T. C. Asmara, M. Yang, G. A. Sawatzky, Y. P. Feng, and A. Rusydi, Interplay of electronic reconstructions, surface oxygen vacancies, and lattice distortions in insulator-metal transition of LaAlO₃/SrTiO₃, *Phys. Rev. B* **92**, 125423 (2015).
- [9] Z. Zhong, A. T  th, and K. Held, Theory of spin-orbit coupling at LaAlO₃/SrTiO₃ interfaces and SrTiO₃ surfaces, *Phys. Rev. B* **87**, 161102(R) (2013).
- [10] N. Mohanta and A. Taraphder, Multiband theory of superconductivity at the LaAlO₃/SrTiO₃ interface, *Phys. Rev. B* **92**, 174531 (2015).
- [11] L. Li, C. Richter, J. Mannhart, and R. Ashoori, Coexistence of magnetic order and two-dimensional superconductivity at LaAlO₃/SrTiO₃ interfaces, *Nat. Phys.* **7**, 762 (2011).
- [12] A. Kalabukhov, R. Gunnarsson, J. Bj  rjesson, E. Olsson, T. Claeson, and D. Winkler, Effect of oxygen vacancies in the SrTiO₃ substrate on the electrical properties of the LaAlO₃/SrTiO₃ interface, *Phys. Rev. B* **75**, 121404(R) (2007).
- [13] N. Mohanta and A. Taraphder, Topological superconductivity and majorana bound states at the LaAlO₃/SrTiO₃ interface, *Europhys. Lett.* **108**, 60001 (2014).
- [14] M. S. Scheurer and J. Schmalian, Topological superconductivity and unconventional pairing in oxide interfaces, *Nat. Commun.* **6**, 6005 (2015).
- [15] S. Nandy, N. Mohanta, S. Acharya, and A. Taraphder, Anomalous transport near the Lifshitz transition at the LaAlO₃/SrTiO₃ interface, *Phys. Rev. B* **94**, 155103 (2016).
- [16] Z. S. Popovi  , S. Satpathy, and R. M. Martin, Origin of the two-dimensional electron gas carrier density at the LaAlO₃ on SrTiO₃ interface, *Phys. Rev. Lett.* **101**, 256801 (2008).
- [17] S. Nandy, G. Sharma, A. Taraphder, and S. Tewari, Chiral anomaly as the origin of the planar hall effect in weyl semimetals, *Phys. Rev. Lett.* **119**, 176804 (2017).
- [18] S. H. Wemple, Some transport properties of oxygen-deficient single-crystal potassium tantalate (KTaO₃), *Phys. Rev.* **137**, A1575 (1965).

- [19] G. E. Jellison, I. Paulauskas, L. A. Boatner, and D. J. Singh, Optical functions of KTaO_3 as determined by spectroscopic ellipsometry and comparison with band structure calculations, *Phys. Rev. B* **74**, 155130 (2006).
- [20] H. Nakamura and T. Kimura, Electric field tuning of spin-orbit coupling in KTaO_3 field-effect transistors, *Phys. Rev. B* **80**, 121308(R) (2009).
- [21] K. V. Shanavas and S. Satpathy, Electric field tuning of the Rashba effect in the polar perovskite structures, *Phys. Rev. Lett.* **112**, 086802 (2014).
- [22] K. Shanavas, Overview of theoretical studies of Rashba effect in polar perovskite surfaces, *J. Electron Spectrosc. Relat. Phenom.* **201**, 121 (2015).
- [23] J. Varignon, M. Bibes, and A. Zunger, Origin of band gaps in 3d perovskite oxides, *Nat. Commun.* **10**, 1658 (2019).
- [24] O. I. Malyi, X.-G. Zhao, and A. Zunger, Insulating band gaps both below and above the Néel temperature in *d*-electron LaTiO_3 , LaVO_3 , SrMnO_3 , and LaMnO_3 perovskites as a symmetry-breaking event, *Phys. Rev. Mater.* **7**, 074406 (2023).
- [25] S. Kakkar and C. Bera, Rashba spin splitting in two-dimensional electron gas in polar-polar perovskite oxide heterostructure $\text{LaVO}_3/\text{KTaO}_3$: A DFT investigation, *Physica E* **144**, 115394 (2022).
- [26] A. Wold and R. Ward, Perovskite-type oxides of cobalt, chromium and vanadium with some rare earth elements, *J. Am. Chem. Soc.* **76**, 1029 (1954).
- [27] L. Jiang, J. Guo, H. Liu, M. Zhu, X. Zhou, P. Wu, and C. Li, Prediction of lattice constant in cubic perovskites, *J. Phys. Chem. Solids* **67**, 1531 (2006).
- [28] P. Bordet, C. Chaillout, M. Marezio, Q. Huang, A. Santoro, S. Cheong, H. Takagi, C. Ogllesby, and B. Batlogg, Structural aspects of the crystallographic-magnetic transition in LaVO_3 around 140 K, *J. Solid State Chem.* **106**, 253 (1993).
- [29] M. De Raychaudhuri, E. Pavarini, and O. K. Andersen, Orbital fluctuations in the different phases of LaVO_3 and YVO_3 , *Phys. Rev. Lett.* **99**, 126402 (2007).
- [30] S. Miyasaka, T. Okuda, and Y. Tokura, Critical behavior of metal-insulator transition in $\text{La}_{1-x}\text{Sr}_x\text{VO}_3$, *Phys. Rev. Lett.* **85**, 5388 (2000).
- [31] Y. Hotta, T. Susaki, and H. Y. Hwang, Polar discontinuity doping of the $\text{LaVO}_3/\text{SrTiO}_3$ interface, *Phys. Rev. Lett.* **99**, 236805 (2007).
- [32] M. Rashid, Z. Abbas, M. Yaseen, Q. Afzal, A. Mahmood, and S. M. Ramay, Theoretical investigation of cubic BaVO_3 and LaVO_3 perovskites via tran-blaha-modified becke-johnson exchange potential approach, *J. Supercond. Novel Magn.* **30**, 3129 (2017).
- [33] U. Lüders, W. C. Sheets, A. David, W. Prellier, and R. Frésard, Room-temperature magnetism in $\text{LaVO}_3/\text{SrVO}_3$ superlattices by geometrically confined doping, *Phys. Rev. B* **80**, 241102(R) (2009).
- [34] H. T. Dang and A. J. Millis, Designing ferromagnetism in vanadium oxide based superlattices, *Phys. Rev. B* **87**, 184434 (2013).
- [35] H. T. Dang and A. J. Millis, Theory of ferromagnetism in vanadium-oxide based perovskites, *Phys. Rev. B* **87**, 155127 (2013).
- [36] G. Kresse and J. Furthmüller, Efficiency of ab-initio total energy calculations for metals and semiconductors using a plane-wave basis set, *Comput. Mater. Sci.* **6**, 15 (1996).
- [37] G. Kresse and J. Furthmüller, Efficient iterative schemes for ab initio total-energy calculations using a plane-wave basis set, *Phys. Rev. B* **54**, 11169 (1996).
- [38] P. E. Blöchl, Projector augmented-wave method, *Phys. Rev. B* **50**, 17953 (1994).
- [39] J. P. Perdew, K. Burke, and M. Ernzerhof, Generalized gradient approximation made simple, *Phys. Rev. Lett.* **77**, 3865 (1996).
- [40] S. L. Dudarev, G. A. Botton, S. Y. Savrasov, C. J. Humphreys, and A. P. Sutton, Electron-energy-loss spectra and the structural stability of nickel oxide: An LSDA + U study, *Phys. Rev. B* **57**, 1505 (1998).
- [41] R. Pentcheva and W. E. Pickett, Ionic relaxation contribution to the electronic reconstruction at the *n*-type $\text{LaAlO}_3/\text{SrTiO}_3$ interface, *Phys. Rev. B* **78**, 205106 (2008).
- [42] V. R. Cooper, Enhanced carrier mobilities in two-dimensional electron gases at III-III/I-V oxide heterostructure interfaces, *Phys. Rev. B* **85**, 235109 (2012).
- [43] E. Assmann, P. Blaha, R. Laskowski, K. Held, S. Okamoto, and G. Sangiovanni, Oxide heterostructures for efficient solar cells, *Phys. Rev. Lett.* **110**, 078701 (2013).
- [44] See Supplemental Material at <http://link.aps.org/supplemental/10.1103/PhysRevB.110.054402> for $\sqrt{2} \times \sqrt{2}$ supercell magnetic calculations, bands for KTO_8 layers, layer projected DOS for 4/4, atomic movements after relaxation, tight-binding bands, and also Tables for relative ground state energies and partial free charges.
- [45] X. Zhang, Z. Pang, C. Yin, M. Yan, Y.-Y. Lv, Y. Deng, and S.-T. Zhang, Quasi-two-dimensional electron gas and weak antiferromagnetism at the interface of $\text{SrTaO}_3/\text{KTaO}_3$ heterostructures, *Phys. Rev. B* **108**, 235114 (2023).
- [46] H. Sawada, N. Hamada, K. Terakura, and T. Asada, Orbital and spin orderings in YVO_3 and LaVO_3 in the generalized gradient approximation, *Phys. Rev. B* **53**, 12742 (1996).
- [47] Z. Fang, N. Nagaosa, and K. Terakura, Anisotropic optical conductivities due to spin and orbital ordering in LaVO_3 and YVO_3 : First-principles studies, *Phys. Rev. B* **67**, 035101 (2003).
- [48] Z. Fang and N. Nagaosa, Quantum versus Jahn-Teller orbital physics in YVO_3 and LaVO_3 , *Phys. Rev. Lett.* **93**, 176404 (2004).
- [49] A. V. Mahajan, D. C. Johnston, D. R. Torgeson, and F. Borsa, Magnetic properties of LaVO_3 , *Phys. Rev. B* **46**, 10966 (1992).
- [50] R. A. de Groot, F. M. Mueller, P. G. van Engen, and K. H. J. Buschow, New class of materials: half-metallic ferromagnets, *Phys. Rev. Lett.* **50**, 2024 (1983).
- [51] S. Picozzi, A. Continenza, and A. Freeman, First principles study of electronic and magnetic properties of $\text{Co}_2\text{MnGe}/\text{GaAs}$ interfaces, *J. Phys. Chem. Solids* **64**, 1697 (2003).
- [52] P. Mavropoulos, M. Ležaić, and S. Blügel, Half-metallic ferromagnets for magnetic tunnel junctions by ab initio calculations, *Phys. Rev. B* **72**, 174428 (2005).
- [53] S. J. Hashemifar, P. Kratzer, and M. Scheffler, Preserving the half-metallicity at the heusler alloy $\text{Co}_2\text{MnSi}(001)$ surface: a density functional theory study, *Phys. Rev. Lett.* **94**, 096402 (2005).
- [54] I. Di Marco, A. Held, S. Keshavarz, Y. O. Kvashnin, and L. Chioncel, Half-metallicity and magnetism in the

- Co₂MnAl/CoMnVAl heterostructure, *Phys. Rev. B* **97**, 035105 (2018).
- [55] S. Jena and S. Datta, Evidence of half-metallicity at the BiFeO₃ (001) surface, *New J. Chem* **47**, 6983 (2023).
- [56] M. J. T. Michael Ziese, *Spin Electronics*, Lecture Notes in Physics (Springer Berlin, Heidelberg, 2001).
- [57] H. Zhang, Z. Zhao, D. Gautreau, M. Raczkowski, A. Saha, V. O. Garlea, H. Cao, T. Hong, H. O. Jeschke, S. D. Mahanti, T. Birol, F. F. Assaad, and X. Ke, Coexistence and interaction of spinons and magnons in an antiferromagnet with alternating antiferromagnetic and ferromagnetic quantum spin chains, *Phys. Rev. Lett.* **125**, 037204 (2020).
- [58] P. W. Anderson, Antiferromagnetism. Theory of superexchange interaction, *Phys. Rev.* **79**, 350 (1950).
- [59] J. B. Goodenough and A. L. Loeb, Theory of ionic ordering, crystal distortion, and magnetic exchange due to covalent forces in spinels, *Phys. Rev.* **98**, 391 (1955).
- [60] J. B. Goodenough, Theory of the role of covalence in the perovskite-type manganites [La, M(II)]MnO₃, *Phys. Rev.* **100**, 564 (1955).
- [61] J. Kanamori, Superexchange interaction and symmetry properties of electron orbitals, *J. Phys. Chem. Solids* **10**, 87 (1959).
- [62] M.-C. Wang and C.-R. Chang, Goodenough-kanamori-anderson rules in CrI₃/MoTe₂/CrI₃ van der Waals heterostructure, *J. Electrochem. Soc.* **169**, 053507 (2022).
- [63] R. D. King-Smith and D. Vanderbilt, Theory of polarization of crystalline solids, *Phys. Rev. B* **47**, 1651 (1993).
- [64] M. Stengel and D. Vanderbilt, Berry-phase theory of polar discontinuities at oxide-oxide interfaces, *Phys. Rev. B* **80**, 241103(R) (2009).
- [65] M. Stengel, First-principles modeling of electrostatically doped perovskite systems, *Phys. Rev. Lett.* **106**, 136803 (2011).